Magnetic solitons in an immiscible two-component Bose-Einstein condensate

Xiao Chai,[1,*] Li You,[2,3] and Chandra Raman[1]

[1]*School of Physics, Georgia Institute of Technology, 837 State Street, Atlanta, Georgia 30332, USA*

[2]*State Key Laboratory of Low Dimensional Quantum Physics, Department of Physics, Tsinghua University, Beijing 100084, China*

[3]*Frontier Science Center for Quantum Information, Beijing 10084, China*

(Received 24 November 2020; accepted 23 December 2021; published 14 January 2022)

We investigate magnetic solitons in an immiscible binary Bose-Einstein condensate (BEC), where the intraspecies interactions are slightly weaker than the interspecies interactions. While their density and phase profiles are analogous to dark-bright solitons, other characteristic properties such as maximum velocities, widths, total density depletions, and in-trap oscillations are different. In the low-velocity regime, a magnetic soliton reduces to a traveling pair of magnetic domain walls. Collisional behaviors of the solitons are also briefly discussed. We further demonstrate that these solitonic states can be realized in a quasi-one-dimensional spin-1 ferromagnetic BEC with a weak spin interaction, e.g., a ^{87}Rb BEC.

DOI: 10.1103/PhysRevA.105.013313

I. INTRODUCTION

Solitons are stable and localized excitations in nonlinear systems. Their stability comes from the combined actions of dispersion and nonlinearity. Solitons exist in various physical systems, such as shallow water [1], optical fibers [2], gravitational systems [3], solid state materials [4], and ultracold atomic quantum gases [5,6]. Systems of ultracold quantum gases stand out as they provide controllable platforms for solitons, and the rich internal structures of ultracold atoms facilitate multicomponent solitons, namely vector solitons. Previous studies of vector solitons in ultracold gases are mostly confined to the Manakov regime [7], with equal intra- and interspecies interaction strengths. Numerous soliton solutions have been obtained, including dark-bright solitons [8,9] in two-component BECs and dark-bright-bright solitons [10–13] in three-component BECs.

The Manakov limit, however, constitutes an approximation for ultracold atomic gases, which is valid provided the spin-dependent or magnetic dynamics are subdominant. In more realistic two-component Bose systems, the intraspecies interaction g_{11}, g_{22} and interspecies interactions g_{12} are usually unequal, so that quantum magnetism can play a role. In the immiscible regime, $\delta g \equiv g - g_{12} < 0$ with $g = \sqrt{g_{11}g_{22}}$, phase separation [14,15] happens spontaneously and magnetic domain walls [16,17], a type of static vector soliton, emerge as a result of modulation instability [18,19]. In the miscible regime where $\delta g > 0$, magnetic solitons, a special type of traveling soliton decoupled from the density dynamics, have been proposed recently [20]. Magnetic solitons are dispersion-free spin density excitations propagating on top of a balanced spin background. Recent experiments indicate that magnetic solitons can be embedded in spin-1 antiferromagnetic BECs of sodium atoms [21–23]. Numerical studies [24] further reveal the existence of correlations between the nonequilibrium spinor dynamics and magnetic solitons.

In this paper, we report on the discovery of another type of traveling soliton in the immiscible regime, which can be considered as the counterpart of the magnetic solitons in the miscible regime [20]. Their properties and existence depend crucially on δg. For consistency with earlier conventions, we will also refer to the traveling solitons we study here as *magnetic solitons*. Similar to Ref. [20], in this work we restrict to the limit $|\delta g| \ll g$ such that the spin and density dynamics are decoupled and the total density can be safely assumed as a constant (see Ref. [25] and Sec. III for more detailed discussions). In reality, this condition is easily fulfilled in a ^{87}Rb BEC where $|\delta g|/g \approx 0.0093$ [26] for a system composed of two hyperfine states $|F = 1, m = \pm 1\rangle$. To our knowledge, solitons in the immiscible regime have only been explored numerically with less analytical insights provided [8,27–29], or studied in the static regime [16,17].

This paper is organized as follows. In Sec. II, we follow the methodology of Ref. [20] and derive the soliton solution in the immiscible regime based on a variational approach. In Sec. III, we study the properties of the soliton and compare them with that of the famous dark-bright soliton. In Sec. IV, we discuss the oscillation of a magnetic soliton when it is embedded in a harmonically trapped condensate. In Sec. V, several collisional behaviors of such solitons are numerically observed, including dimer formation and polarization flip. In Sec. VI, a method for the experimental generation of magnetic solitons in a ^{87}Rb BEC is proposed, based on the phase imprinting approach developed recently [21].

II. FORMALISM AND SOLUTION

For a one-dimensional (1D) binary BEC, its mean-field equations of motion can be obtained from the Lagrangian density (see Appendices A–C),

$$\mathcal{L} = \sum_{j=1}^{2} \frac{i\hbar}{2}\left(\psi_j^* \frac{\partial \psi_j}{\partial t} - \psi_j \frac{\partial \psi_j^*}{\partial t}\right) - \mathcal{E}, \tag{1}$$

*xchai@gatech.edu

where $\psi_j(z,t)$ is the jth component condensate wave function with $j=1,2$, and z,t are space and time coordinates, respectively. $\mathcal{E}$ is the energy density given by

$$\mathcal{E}=\sum_{j=1}^{2}\left(\frac{\hbar^2}{2M}\left|\frac{\partial\psi_j}{\partial z}\right|^2+\mathcal{V}|\psi_j|^2+\sum_{l=1}^{2}\frac{g_{jl}}{2}|\psi_j|^2|\psi_l|^2\right), \quad (2)$$

with M the same atomic mass of both components, and $\mathcal{V}(z)$ the trapping potential. We will focus on the parameter regime where $g_{11}=g_{22}=g=g_{12}+\delta g=g_{21}+\delta g$ with $\delta g<0$. The wave functions can be parametrized as

$$\begin{pmatrix}\psi_1\\ \psi_2\end{pmatrix}=\sqrt{\mathfrak{n}}\begin{pmatrix}\cos(\theta/2)e^{i\phi_1}\\ \sin(\theta/2)e^{i\phi_2}\end{pmatrix}, \quad (3)$$

where $\theta(z,t),\phi_j(z,t)$ are real and $\mathfrak{n}(z,t)>0$. In the following discussion we *assume* the total density $\mathfrak{n}(z,t)$ is a constant n. To search for traveling soliton solutions with a constant velocity V, we write $\theta(z,t)=\theta(z-Vt)$ and $\phi_j(z,t)=\phi_j(z-Vt)$. Then in the uniform case with $\mathcal{V}=0$, the Lagrangian (1) can be expressed as

$$\begin{aligned}\frac{\mathcal{L}}{nMV_s^2}=&\frac{1}{16}\cos 2\theta-\frac{1}{8}(\partial_\zeta\theta)^2+\frac{1}{2}U(1+\cos\theta)\partial_\zeta\phi_1\\&-\frac{1}{4}(1+\cos\theta)(\partial_\zeta\phi_1)^2+\frac{1}{2}U(1-\cos\theta)\partial_\zeta\phi_2\\&-\frac{1}{4}(1-\cos\theta)(\partial_\zeta\phi_2)^2, \quad (4)\end{aligned}$$

where $\zeta=(z-Vt)/\xi_s$ and $U=V/V_s$ are the normalized moving coordinate and velocity, respectively. $\xi_s=\hbar/\sqrt{2Mn|\delta g|}$ is the spin healing length and $V_s=\sqrt{2n|\delta g|/M}$ is in fact the maximum speed of the soliton, as it will become clear later. Our definition for ξ_s differs from the choice of Ref. [30]. We also omit constant terms in $\mathcal{L}$ which do not contribute to the dynamics.

Due to the immiscible nature the background of the soliton is fully spin polarized, which means only one spin component (e.g., the component 1) exists at infinity and the other spin component is localized. Thus we impose the following boundary conditions for θ,

$$\theta=\partial_\zeta\theta=0, \quad \text{at } \zeta\to\pm\infty. \quad (5)$$

When a global flux is absent for the component 1, the boundary condition for $\partial_\zeta\phi_1$ is given by

$$\partial_\zeta\phi_1=0, \quad \text{at } \zeta\to\pm\infty. \quad (6)$$

No restriction for $\partial_\zeta\phi_2$ is supplied at infinity because the component 2 has no population at infinity.

The variation of the Lagrangian with respect to ϕ_1 gives

$$\partial_\zeta\{-U\cos\theta+(1+\cos\theta)\partial_\zeta\phi_1\}=0. \quad (7)$$

Applying the boundary conditions (5) and (6) we find

$$\partial_\zeta\phi_1=-U\frac{1-\cos\theta}{1+\cos\theta}. \quad (8)$$

The variation with respect to ϕ_2 gives additionally

$$\partial_\zeta\{U\cos\theta+(1-\cos\theta)\partial_\zeta\phi_2\}=0. \quad (9)$$

Assuming an integration constant C_0 for the above equation gives

$$\partial_\zeta\phi_2=\frac{C_0-U\cos\theta}{1-\cos\theta}. \quad (10)$$

Varying $\mathcal{L}$ with respect to θ we find

$$\begin{aligned}\partial_\zeta^2\theta=&\sin\theta\{\cos\theta+2U\partial_\zeta\phi_1-(\partial_\zeta\phi_1)^2\\&-2U\partial_\zeta\phi_2+(\partial_\zeta\phi_2)^2\}. \quad (11)\end{aligned}$$

To avoid divergence of $\partial_\zeta^2\theta$ at infinity, $\partial_\zeta\phi_2$ must be finite at infinity, which results in the restriction $C_0=U$ and leads to

$$\partial_\zeta\phi_2=U. \quad (12)$$

Simplifying Eq. (11) with Eqs. (8) and (12) we obtain

$$\partial_\zeta^2\theta=-U^2\frac{\sin\theta}{\cos^4(\theta/2)}+\sin\theta\cos\theta, \quad (13)$$

whose integration gives the densities of each component,

$$\begin{aligned}\frac{n_1}{n}&=\frac{1}{2}(1+\cos\theta)=1-\frac{1-U^2}{1+|U|\cosh(2\sqrt{1-U^2}\zeta)},\\ \frac{n_2}{n}&=\frac{1}{2}(1-\cos\theta)=\frac{1-U^2}{1+|U|\cosh(2\sqrt{1-U^2}\zeta)}. \quad (14)\end{aligned}$$

Further integrating Eqs. (8) and (12) gives the phases of both components,

$$\begin{aligned}\phi_1&=-\mathrm{sgn}(U)\arctan\left(\frac{(1-|U|)\tanh(\sqrt{1-U^2}\zeta)}{\sqrt{1-U^2}}\right)+C,\\ \phi_2&=U\zeta+\Phi, \quad (15)\end{aligned}$$

where the constant C ensures $\phi_1(\zeta=-\infty)=0$ to fix the U(1) gauge. Φ is a constant phase shift of the component 2. Equations (14) and (15) constitute the principle result of this work. This result can be mapped to a soliton solution of the Landau-Lifshitz equation for easy-axis ferromagnets [31].

III. SOLITON PROPERTIES

The soliton solutions (14) and (15) are parametrized by U and Φ. The phase shift Φ is only relevant when there exist two or more solitons, so it will be left aside for now, while $U=V/V_s$ can take values in $-1\leqslant U\leqslant 1$. The maximum speed of the soliton is $V_s=\sqrt{2n|\delta g|/M}$, which differs from the miscible case by a factor of 2 [20]. Typical density and phase distributions of a magnetic soliton with immiscible surrounding condensate are shown in Figs. 1(a) and 1(b), for $U=0.3$ and $\Phi=0$. The soliton exhibits a density notch for the component 1, which is filled by a density bump for the component 2. The component 2 displays a linear phase with slope U/ξ_s, while the component 1 is featured for its phase jump $\Delta\phi_1$ across the soliton, which approaches $\pi/2$ when $U\to 0$ and vanishes when $U\to\pm 1$ [see Fig. 1(d)]. The slope of the phase difference $\partial_z(\phi_2-\phi_1)$ at the soliton center is $\mathrm{sgn}(U)/\xi_s$, independent of the speed.

Similar to the magnetic soliton we discuss here, the dark-bright soliton studied by Busch and Anglin [8] comes with a dark component filled by a bright component, and its phase profiles are akin to that of magnetic solitons as well. Nevertheless, significant differences exist in several aspects. First

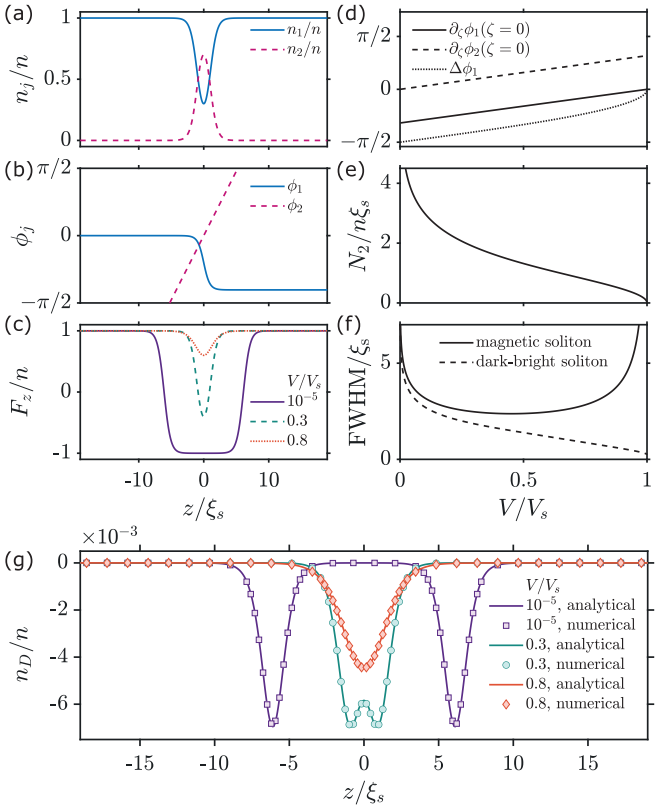

FIG. 1. (a), (b) Profile of a magnetic soliton with $U = 0.3$ and $\Phi = 0$. The blue solid and red dashed curves are (a) density or (b) phase profiles of the two components, respectively. (c) Spin density of a magnetic soliton with various velocities. The purple solid line, green dashed line, and orange dotted line represent the spin densities of a soliton with $U = 10^{-5}$, 0.3, and 0.8, respectively. (d) Dependence of the soliton phases on the soliton velocity. The solid and the dashed lines are slopes of ϕ_1, ϕ_2 at the center of the soliton, respectively. The dotted curve is the phase jump $\Delta\phi_1 = \phi_1(\zeta = +\infty) - \phi_1(\zeta = -\infty)$. (e) Total population of the component 2 in a magnetic soliton. (f) Full width half maximum (FWHM) of the magnetic soliton (dashed line) and the dark-bright soliton (solid line). (g) Density depletion of the magnetic soliton. The solid lines and points represent analytical and numerical results, respectively.

and most importantly, the dark-bright soliton is developed under the Manakov regime where $\delta g = 0$, while the immiscible magnetic soliton can only exist when δg is negative. As a consequence, the properties of a magnetic soliton depend solely on δg instead of g. For example, the speed of a dark-bright soliton is regulated by the sound velocity $c_n = \sqrt{ng/M}$, while the speed of a magnetic soliton is limited by $V_s = \sqrt{2n|\delta g|/M}$, which is smaller by $\sqrt{2|\delta g|/g} \approx 13.6\%$. Here, we have used $|\delta g|/g \approx 0.0093$ for the ground-state ^{87}Rb condensate in $|F = 1, m = \pm1\rangle$, and this ratio will be assumed in the following discussion.

Second, in the low-velocity limit the magnetic soliton exhibits intriguing behaviors unseen in the dark-bright soliton. As shown in Fig. 1(c), the spin density (defined as $F_z \equiv n_1 - n_2$) of a magnetic soliton has a notch. As the velocity approaches zero, the notch becomes deeper and larger, and eventually it develops into a pair of magnetic domain walls. Indeed, in the limit $U \to 0^+$ the spin density is given by

$$\frac{F_z}{n} \approx 1 + \tanh(\zeta - \zeta_0/2) - \tanh(\zeta + \zeta_0/2), \tag{16}$$

where $\zeta_0\xi_s = \xi_s \ln(2/U)$ is the separation between the two domain walls. As U gets closer to zero, the separation increases significantly beyond ξ_s, the width of the domain walls, and eventually the background spin is flipped when $U = 0$. We note that the hyperbolic tangent shape of each of these domain walls is coincident with a recent domain wall study [17] as well as the earlier work [29,31,32].

Third, we consider the bright component population and the soliton size. Unlike the dark-bright soliton, the bright component atom number of a magnetic soliton is not a free parameter, but is dependent on its velocity as

$$N_2 = n\xi_s \ln[|U|/(1 - \sqrt{1 - U^2})]. \tag{17}$$

As shown in Fig. 1(e), N_2 diverges when $U \to 0$ and vanishes when $U = \pm1$. Assuming the dark-bright soliton and the magnetic soliton have the same bright component population, we compare their full width half maximum (FWHM) in Fig. 1(f). The FWHM of a magnetic soliton reaches its minimum value $2.37\xi_s$ at $U \approx \pm0.45$ and diverges at $U \to \pm1$ or $U \to 0$, while the FWHM of a dark-bright soliton monotonically decreases as its velocity increases.

Finally, we revisit the uniform density approximation. Consider a parametrization for the condensate wave functions beyond the uniform density approximation,

$$\begin{pmatrix}\psi_1\\ \psi_2\end{pmatrix} = \sqrt{\mathfrak{n}}\begin{pmatrix}\cos(\theta/2)e^{i\phi_1}\\ \sin(\theta/2)e^{i\phi_2}\end{pmatrix}e^{-i\mu t/\hbar}, \tag{18}$$

where $\mu = ng$ is the chemical potential at equilibrium with only one component present at density n. $\mathfrak{n}(z,t)$ is the total density as a function of space and time. Using dimensionless variables $\mathcal{Z} = z/\xi_s$ and $\mathcal{T} = t/t_s$, we find the Lagrangian (1) is reduced to

$$\begin{aligned}\frac{\mathcal{L}}{nMV_s^2} =& -\frac{g}{4n^2\delta g}(\mathfrak{n}^2 - 2n\mathfrak{n}) \\ &- \frac{1}{8n^2}\Big\{\mathfrak{n}^2\sin^2\theta + \frac{n(\partial_{\mathcal{Z}}\mathfrak{n})^2}{\mathfrak{n}} + n\mathfrak{n}(\partial_{\mathcal{Z}}\theta)^2 \\ &+4n\mathfrak{n}(1+\cos\theta)\partial_{\mathcal{T}}\phi_1 + 4n\mathfrak{n}(1-\cos\theta)\partial_{\mathcal{T}}\phi_2 \\ &+2n\mathfrak{n}(1+\cos\theta)(\partial_{\mathcal{Z}}\phi_1)^2 \\ &+2n\mathfrak{n}(1-\cos\theta)(\partial_{\mathcal{Z}}\phi_2)^2\Big\},\end{aligned} \tag{19}$$

in the absence of a trapping potential. Variation of the Lagrangian with respect to $\mathfrak{n}$ gives

$$\begin{aligned}\frac{\mathfrak{n}-n}{n} =& \frac{\delta g}{2g}\Big\{\frac{\mathfrak{n}\sin^2\theta}{n} + \frac{(\partial_{\mathcal{Z}}\mathfrak{n})^2}{2\mathfrak{n}^2} - \frac{\partial^2_{\mathcal{Z}}\mathfrak{n}}{\mathfrak{n}} + \frac{1}{2}(\partial_{\mathcal{Z}}\theta)^2 \\ &+2(1+\cos\theta)\partial_{\mathcal{T}}\phi_1 + 2(1-\cos\theta)\partial_{\mathcal{T}}\phi_2 \\ &+(1+\cos\theta)(\partial_{\mathcal{Z}}\phi_1)^2 + (1-\cos\theta)(\partial_{\mathcal{Z}}\phi_2)^2\Big\}.\end{aligned} \tag{20}$$

The right-hand side (RHS) of the above equation becomes negligible when $|\delta g|/g \ll 1$ such that $\mathfrak{n} \approx n$ at the leading

order, which validates our uniform density approximation. Inserting the magnetic soliton solution (14) and (15) into the RHS of the above equation, we find the asymptotic density depletion n_D as the first-order correction,

$$\frac{n_D}{n} = \frac{\mathfrak{n} - n}{n} \approx \frac{3\delta g}{g} \frac{|U|(1-U^2)[|U| + \cosh(2\sqrt{1-U^2}\zeta)]}{[1+|U|\cosh(2\sqrt{1-U^2}\zeta)]^2}, \tag{21}$$

where $\zeta = \mathcal{Z} - U\mathcal{T}$. Then the total population depletion becomes

$$N_D = \int d\zeta n_D \xi_s \approx \frac{3n\delta g}{g}\sqrt{1-U^2}\xi_s. \tag{22}$$

We compare Eq. (21) with numerical results obtained from the moving frame Newton-Raphson method [33–35] (see Appendixes D and E). The numerical and analytical results match very well as illustrated in Fig. 1(g). The density depletion $n_D/n \sim 10^{-3}$ validates the uniform density approximation. At low soliton velocity, n_D displays a double-dip local core structure with each dip matching the density depletion of a single magnetic domain wall as discovered by Yu and Blakie [17]. In comparison, the total density of a dark-bright soliton always displays a dark soliton shape [8].

IV. ENERGY AND IN-TRAP OSCILLATION

The energy of a soliton can be evaluated as the difference of the total energy $\int \mathcal{E} dz$ in the presence or absence of the soliton [36]. Direct calculation gives the energy $\epsilon = n\hbar V_s\sqrt{1-U^2}$ for a magnetic soliton in a uniform system, when $U \neq 0$, (when $U = 0$, the energy is zero). The effective mass at small soliton velocity is $m_{\text{eff}} = -n\hbar/V_s$, which is negative, implicating the presence of snake instability [37]. However, the relatively large soliton size ($>2.37\xi_s$) establishes a marginal robustness of the solitons against transverse excitations in a quasi-1D BEC.

The energy of a magnetic soliton in the immiscible regime exhibits the same form as in the miscible case [20], although in contrast to the miscible case, the local density approximation (LDA) for the soliton energy [38] fails to predict the in-trap oscillation of a magnetic soliton in the immiscible regime we study here. Following the same procedure in Refs. [20,38], we find the LDA gives the oscillation amplitude L and period T of the magnetic soliton as

$$\frac{L}{R_z} = \sqrt{1-(1-U_0^2)^{1/3}}, \tag{23}$$

$$\frac{T}{T_z} = \frac{2}{\pi}\sqrt{\frac{g}{|\delta g|}}\int_0^{L/R_z} \frac{v(\beta)d\beta}{\sqrt{v^3(\beta)-1+U_0^2}}, \tag{24}$$

where R_z, T_z are the Thomas-Fermi radius and trapping period. $v(\beta) = 1-\beta^2$. U_0 is the normalized soliton velocity at the center of the trap. As shown in Fig. 2, the numerical results disobey the LDA prediction.

We attribute this discrepancy to the dependence of N_2 on the soliton velocity in the immiscible case. Both ϵ and N_2 are integrals of motion of the original Lagrangian (1) when $\mathcal{V}$ is nonzero, but the LDA cannot simultaneously guarantee the conservation of these two quantities when the magnetic soliton oscillates in a trap with varying velocity. In fact, the shape of the soliton deforms when the soliton approaches the oscillation turning point, where the assumption of LDA is no longer valid. For comparison, the oscillation amplitude and period of a dark-bright soliton are also displayed in Fig. 2, and the bright component population is assumed to be the same as that of the magnetic soliton.

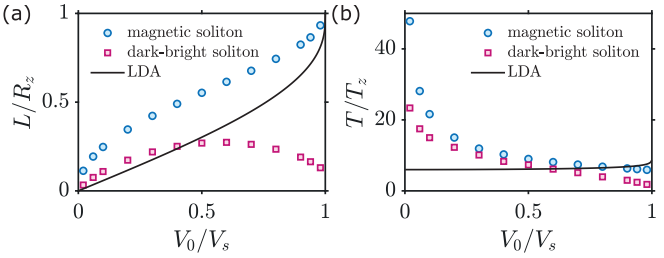

FIG. 2. Oscillations of a magnetic soliton and a dark-bright soliton in a harmonic trap are compared. The blue circles and red squares are numerical results for the magnetic soliton and the dark-bright soliton, respectively. The black curve is the local density approximation (LDA) prediction for the magnetic soliton. V_0 is the soliton velocity at the center of the condensate. In (a) we show the oscillation amplitude L normalized to the Thomas-Fermi radius $R_z = \sqrt{2n_0 g/M\omega_z^2}$, where ω_z and n_0 are the trapping frequency and density at the center. In (b) we show the oscillation period normalized to the trap period $T_z = 2\pi/\omega_z$.

V. COLLISION

Collisions between two magnetic solitons in an immiscible BEC depend on their phase Φ. In numerical simulations, we imprint two magnetic solitons moving towards each other in a uniform BEC. As shown in Fig. 3(a), if the phase difference between the two solitons is zero, i.e., $\Delta\Phi = 0$, the two solitons are found to attract each other during collision. When $\Delta\Phi = \pi$ the two solitons repel each other, as illustrated in Fig. 3(b). Such a behavior is similar to collisions of dark-bright solitons [8]. A magnetic soliton dimer can form after collision, if initially the two solitons overlap spatially and their phase difference is zero, as shown in Fig. 3(c). In contrast, when there is no overlap the two solitons bounce off each other as seen in Fig. 3(d). For nonzero phase difference the overlapped two-soliton initial state cannot be constructed without perturbing the background condensate.

Next, we engineer collisions between a magnetic soliton and a tanh-shaped domain wall [17]. Figure 3(e) shows that after collision the magnetic soliton penetrates the domain wall and its polarization is flipped. The location of the domain wall is also shifted after the collision. Collision between a traveling magnetic soliton and a quasistatic magnetic soliton (domain wall pair) displays similar dynamics, as shown in Fig. 3(f), although after collision the traveling soliton retrieves its initial shape.

VI. EXPERIMENTAL GENERATION

Here, we propose a method to experimentally generate a magnetic soliton in a ferromagnetic spin-1 BEC, where the two components are taken as the $m = \pm 1$ states. To eliminate the $m = 0$ component, one may introduce a negative quadratic

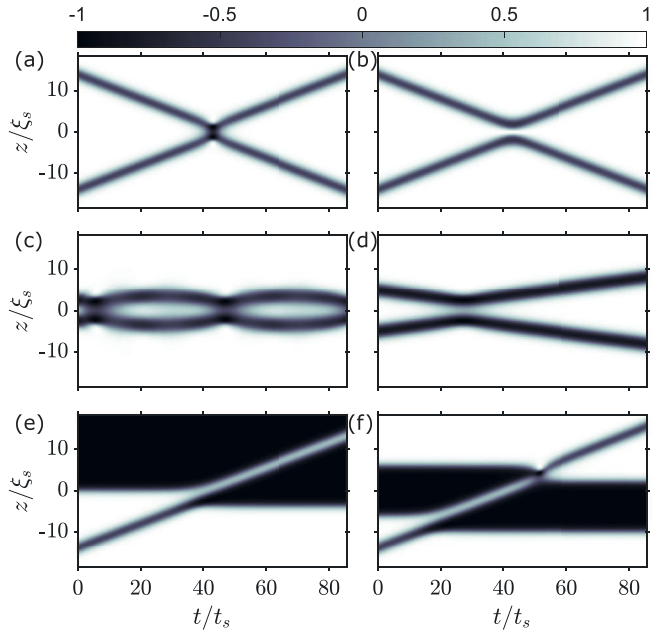

FIG. 3. Soliton collisions in a uniform system. Plots show the normalized spin density $F_z/n = (n_1 - n_2)/n$ as a function of space and time. The timescale is $t_s = \xi_s/V_s$. In (a) and (b), $|U| = 0.3$ for both solitons. The phase differences are (a) $\Delta\Phi = 0$, and (b) $\Delta\Phi = \pi$. (c) shows the formation of a magnetic soliton dimer after collision, where initially $|U| = 0.1$ for both solitons and the separation is $5\xi_s$. (d) is in comparison with (c) where $|U| = 0.1$ but the separation is $10\xi_s$. (e) shows the collision between a magnetic soliton with $|U| = 0.3$ and a static domain wall. (f) shows the collision between two magnetic solitons with $|U| = 0.3$ and $|U| = 10^{-5}$.

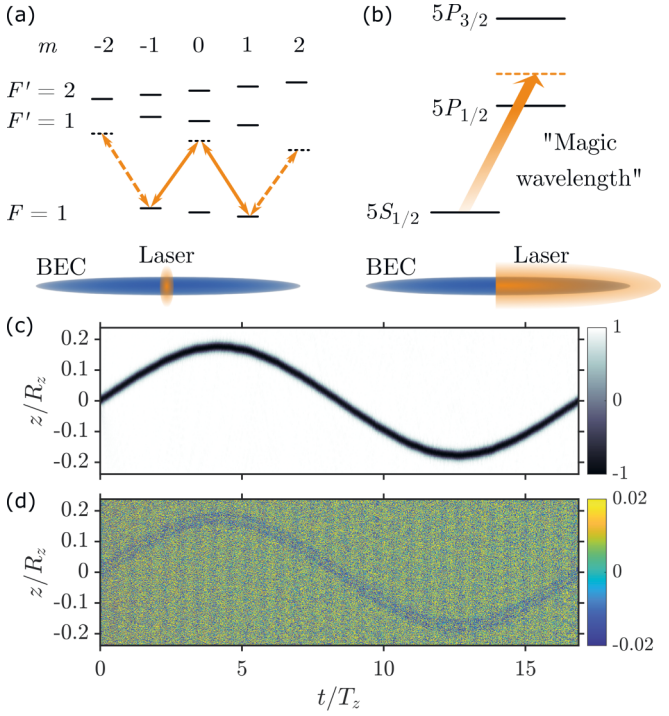

FIG. 4. Proposal to generate a magnetic soliton in a quasi-1D ^{87}Rb BEC. (a) Local population transfer from $m = 1$ to $m = -1$. A Raman laser pulse coupling the $5S_{1/2}, |F = 1, m = \pm 1\rangle$ states through the $5P_{1/2}$ state illuminates the center of the condensate. The pulse duration is controlled to transfer a desired fraction of atoms. (b) Magnetic shadow. An enlarged laser beam is imaged onto half of the condensate. The laser frequency is tuned to the "magic frequency" so that it only induces a vector ac Stark shift. The laser beam is pulsed such that a finite phase jump is generated. (c) Oscillation of the generated magnetic soliton in a harmonic trap. The plot shows the normalized spin density $[n_{+1}(z,t) - n_{-1}(z,t)]/\mathfrak{n}(z,t)$ as a function of space and time, where $n_{\pm 1}(z,t)$ are the densities of the $m = \pm 1$ components. (d) Plot of the normalized density depletion defined as $[\mathfrak{n}(z,t) - \mathfrak{n}_g(z)]/\mathfrak{n}_g(z)$, where $\mathfrak{n}_g(z)$ is the ground-state density distribution.

Zeeman shift q, such that the condensate is forced to stay in the ferromagnetic phase [30]. The length scale of the soliton is characterized by the spin healing length ξ_s. Using typical experimental conditions for a quasi-1D ^{87}Rb BEC [12], we find the minimum width of a magnetic soliton is $2.37\xi_s \approx 9.2\ \mu$m. To avoid snake instability [37], the transverse size of the quasi-1D BEC must be made smaller.

Suppose initially the condensate is prepared in a ferromagnetic state with all the atoms in the $m = 1$ state and stabilized by a negative quadratic Zeeman shift. To generate a magnetic soliton we first apply a local population transfer from $m = 1$ to $m = -1$, which can be accomplished by a focused Raman laser pulse [39], as shown in Fig. 4(a). Subsequently a magnetic shadow [21] [see Fig. 4(b)] is cast to induce a phase difference, leading to a local relative superfluid velocity between the two components. The relative superfluid velocity then helps to assist in the formation of a magnetic soliton.

The above procedure is confirmed in a numerical simulation (see Appendix F) and indeed a single magnetic soliton is generated which subsequently oscillates in a harmonic trap, as shown in Fig. 4(c). To be more realistic, we include Gaussian noise and a negative quadratic Zeeman shift in our simulation. The density depletion of the generated soliton, shown in Fig. 4(d), displays a double-dip core structure, which is a characteristic feature of the magnetic soliton. The fringes in Fig. 4(d) are density waves as by-products of our procedure.

VII. CONCLUSION AND OUTLOOK

We have derived a closed-form magnetic soliton solution for the coupled two-component Gross-Pitaevskii equations with $\delta g < 0$. We hope our results will stimulate experimental studies. Though the solution is obtained in a two-component system, it can be extended to a broader class of soliton solutions in a spin-1 system by exploiting the underlying SO(3) symmetry [17,23]. The correlation between the quench dynamics of a ferromagnetic spin-1 condensate [40] and magnetic solitons is an interesting topic worthy of some immediate studies. Other unsolved problems, including the dynamical stability in higher dimensions and the in-trap oscillation of a magnetic soliton, remain to be explored in the future.

ACKNOWLEDGMENTS

We are thankful for fruitful discussions with Kazuya Fujimoto, Di Lao, Feng Chen, and Chao Li. X.C. and C.R. acknowledge the support from the National Science

Foundation through Award No. 2011478. L.Y. acknowledges the support from the National Key R&D Program of China (Grant No. 2018YFA0306504), and from the National Natural Science Foundation of China (NSFC) (No. 11654001 and No. U1930201).

APPENDIX A: SPIN-1 GROSS-PITAEVSKII EQUATIONS IN 3D

A spin-1 BEC at zero temperature can be well described by a spinor wave function $\Psi_m(\boldsymbol{r},t)$, where $m=-1,0,+1$ is the magnetic quantum number and $\boldsymbol{r},t$ are space and time coordinates, respectively. The dynamics of $\Psi_m(\boldsymbol{r},t)$ is governed by three coupled Gross-Pitaevskii equations (GPEs),

$$i\hbar\frac{\partial}{\partial t}\Psi_m=\left(-\frac{\hbar^2}{2M}\nabla^2+\mathcal{V}\right)\Psi_m+qm^2\Psi_m+c_0\mathfrak{n}\Psi_m+c_2\sum_{n=-1}^{1}\boldsymbol{F}\cdot(\hat{\boldsymbol{F}})_{mn}\Psi_n, \tag{A1}$$

where M is the atomic mass. $\mathcal{V}(\boldsymbol{r})$ and q are the spin-independent potential and the quadratic Zeeman shift, respectively. $\mathfrak{n}(\boldsymbol{r},t)=\sum_{m=-1}^{1}|\Psi_m(\boldsymbol{r},t)|^2$ is the total density. The wave function is normalized to the total number of atoms as $\int d\boldsymbol{r}\mathfrak{n}(\boldsymbol{r},t)=N$. c_0,c_2 are spin-independent and spin-dependent interaction coupling constants defined as $c_0=4\pi\hbar^2(a_2+2a_0)/3M$ and $c_2=4\pi\hbar^2(a_2-a_0)/3M$, where a_0,a_2 are s-wave scattering lengths of collisions in the total $F=0,2$ channels. We consider ferromagnetic interactions only in this study such that $c_2<0<c_0$. $\boldsymbol{F}(\boldsymbol{r},t)=\sum_{m,n=-1}^{1}\Psi_m^*(\boldsymbol{r},t)(\hat{\boldsymbol{F}})_{mn}\Psi_n(\boldsymbol{r},t)$ is the spin density and $\hat{\boldsymbol{F}}=(\hat{F}_x,\hat{F}_y,\hat{F}_z)^T$ with $\hat{F}_x,\hat{F}_y,\hat{F}_z$ being the spin-1 matrices,

$$\hat{F}_x=\frac{1}{\sqrt{2}}\begin{pmatrix}0&1&0\\1&0&1\\0&1&0\end{pmatrix},\quad \hat{F}_y=\frac{i}{\sqrt{2}}\begin{pmatrix}0&-1&0\\1&0&-1\\0&1&0\end{pmatrix},\quad \hat{F}_z=\begin{pmatrix}1&0&0\\0&0&0\\0&0&-1\end{pmatrix}. \tag{A2}$$

In experiments, BECs are usually trapped optically and the trapping potential $\mathcal{V}(\boldsymbol{r})$ can be approximated as a harmonic potential. We use experimental parameters from Ref. [12] where the cigar-shaped trap has frequencies $\{\omega_x,\omega_y,\omega_z\}=2\pi\times\{176,174,1.4\}$ Hz (we have changed the labels for consistency with our paper). With $N=0.8\times10^6$ atoms in the BEC, the Thomas-Fermi radii are $\{R_x,R_y,R_z\}=\{3,3,369\}$ μm.

APPENDIX B: SPIN-1 GROSS-PITAEVSKII EQUATIONS IN 1D

For a cigar-shaped condensate with $\omega_x\gg\omega_z$ and $\omega_y\gg\omega_z$, one can assume that the wave function can be written as

$$\Psi_m(\boldsymbol{r},t)=\Psi_m^{(1\mathrm{D})}(z,t)G(x,y), \tag{B1}$$

where $G(x,y)$ is the transverse wave function in the Thomas-Fermi limit:

$$G(x,y)=\begin{cases}\sqrt{\frac{2}{\pi R_xR_y}\left(1-\frac{x^2}{R_x^2}-\frac{y^2}{R_y^2}\right)}, & \frac{x^2}{R_x^2}+\frac{y^2}{R_y^2}\leqslant 1,\\ 0, & \text{otherwise.}\end{cases} \tag{B2}$$

$G(x,y)$ and $\Psi_m^{(1\mathrm{D})}(z,t)$ are normalized independently as $\int dxdy|G(x,y)|^2=1$ and $\int dz\sum_{m=-1}^{1}|\Psi_m^{(1\mathrm{D})}(z,t)|^2=N$. The 3D GPEs (A1) can then be reduced to

$$i\hbar\frac{\partial}{\partial t}\Psi_m^{(1\mathrm{D})}=\left(-\frac{\hbar^2}{2M}\frac{\partial^2}{\partial z^2}+\mathcal{V}^{(1\mathrm{D})}\right)\Psi_m^{(1\mathrm{D})}+qm^2\Psi_m^{(1\mathrm{D})}+g_0\mathfrak{n}^{(1\mathrm{D})}\Psi_m^{(1\mathrm{D})}+g_2\sum_{n=-1}^{1}\boldsymbol{F}^{(1\mathrm{D})}\cdot(\hat{\boldsymbol{F}})_{mn}\Psi_n^{(1\mathrm{D})}, \tag{B3}$$

where g_0,g_2 are effective coupling constants in 1D given by $g_0=4c_0/3\pi R_xR_y$ and $g_2=4c_2/3\pi R_xR_y$. The definitions for total density and spin density in 1D are given accordingly as $\mathfrak{n}^{(1\mathrm{D})}(z,t)=\sum_{m=-1}^{1}|\Psi_m^{(1\mathrm{D})}(z,t)|^2$ and $\boldsymbol{F}^{(1\mathrm{D})}(z,t)=\sum_{m,n=-1}^{1}\Psi_m^{(1\mathrm{D})*}(z,t)(\hat{\boldsymbol{F}})_{mn}\Psi_n^{(1\mathrm{D})}(z,t)$. $\mathcal{V}^{(1\mathrm{D})}(z)=M\omega_z^2z^2/2$ is the spin-independent potential in the presence of a harmonic trap.

APPENDIX C: BINARY GROSS-PITAEVSKII EQUATIONS IN 1D

Experimentally one can use microwave dressing to apply a negative quadratic Zeeman shift. Hence the energy of $m=\pm1$ states is lowered so that the spin exchange collision $|1,1\rangle+|1,-1\rangle\to2|1,0\rangle$ can be suppressed. With $m=0$ atoms eliminated, the spin-1 GPEs (B3) reduce to the binary GPEs,

$$i\hbar\frac{\partial}{\partial t}\psi_1=\left(-\frac{\hbar^2}{2M}\frac{\partial^2}{\partial z^2}+\mathcal{V}^{(1\mathrm{D})}+g_{11}|\psi_1|^2+g_{12}|\psi_2|^2\right)\psi_1,$$
$$i\hbar\frac{\partial}{\partial t}\psi_2=\left(-\frac{\hbar^2}{2M}\frac{\partial^2}{\partial z^2}+\mathcal{V}^{(1\mathrm{D})}+g_{22}|\psi_2|^2+g_{12}|\psi_1|^2\right)\psi_2, \tag{C1}$$

where $\psi_1\equiv\Psi_{+1}^{(1\mathrm{D})}$ and $\psi_2\equiv\Psi_{-1}^{(1\mathrm{D})}$. $g_{11}=g_{22}=g_0+g_2=g$ are the intraspecies interaction strengths. $g_{12}=g_0-g_2=g-\delta g$ is the interspecies interaction strengths. The quadratic Zeeman shift term has been eliminated because it only introduces a constant energy shift for the two states $m=\pm1$. Equations (C1) can be derived from the Lagrangian given in the main text, provided that the label (1D) is removed.

APPENDIX D: DIMENSIONLESS SPIN-1 GPES IN 1D

We choose $z_0=\sqrt{\hbar/\omega_zM}$, $t_0=1/\omega_z$, and $\epsilon_0=\hbar\omega_z$ as our length, time, and energy scales, respectively. Then the dimensionless spin-1 GPEs are written as

$$i\frac{\partial}{\partial\tilde{t}}\tilde{\Psi}_m=\left(-\frac{1}{2}\frac{\partial^2}{\partial\tilde{z}^2}+\tilde{\mathcal{V}}\right)\tilde{\Psi}_m+\tilde{q}m^2\tilde{\Psi}_m+\tilde{g}_0\tilde{\mathfrak{n}}\tilde{\Psi}_m+\tilde{g}_2\sum_{n=-1}^{1}\tilde{\boldsymbol{F}}\cdot(\hat{\boldsymbol{F}})_{mn}\tilde{\Psi}_n, \tag{D1}$$

where the dimensionless quantities are given in the following,

$$\tilde{z} = \frac{z}{z_0}, \quad \tilde{t} = \frac{t}{t_0}, \quad \tilde{\mathcal{V}} = \frac{\mathcal{V}^{(1D)}}{\epsilon_0}, \quad \tilde{q} = \frac{q}{\epsilon_0},$$
$$\tilde{g}_0 = \frac{g_0 N}{x_0 \epsilon_0}, \quad \tilde{g}_2 = \frac{g_2 N}{x_0 \epsilon_0},$$
$$\tilde{\Psi}_m = \sqrt{\frac{x_0}{N}}\Psi_m^{(1D)}, \quad \tilde{\mathfrak{n}} = \frac{x_0}{N}\mathfrak{n}^{(1D)}, \quad \tilde{\boldsymbol{F}} = \frac{x_0}{N}\boldsymbol{F}^{(1D)}. \tag{D2}$$

The dimensionless wave function is normalized as $\int d\tilde{z} \sum_{m=-1}^{1} |\tilde{\Psi}_m(\tilde{z},\tilde{t})|^2 = 1$. Using typical experimental parameters in Ref. [12] and scattering length data in Ref. [26], we find the nonlinear coefficients are $\tilde{g}_0 = 23\,729$ and $\tilde{g}_2 = -110$. Equation (D1) can then be integrated numerically using, for example, the time-splitting spectral method.

APPENDIX E: NEWTON-RAPHSON METHOD

Here, we discuss how we numerically obtain the magnetic soliton solutions beyond the uniform density approximation. Consider a stationary soliton solution of the GPEs (D1),

$$\tilde{\Psi}_m(\tilde{z},\tilde{t}) = \tilde{\Psi}_m(\tilde{z}) e^{-i\tilde{\mu}\tilde{t}}, \tag{E1}$$

where $\tilde{\mu}$ is the dimensionless chemical potential. Substituting Eq. (E1) back into Eq. (D1), we have the time-independent GPEs,

$$\tilde{\mu}\tilde{\Psi}_m = \left(-\frac{1}{2}\frac{\partial^2}{\partial\tilde{z}^2} + \tilde{\mathcal{V}}\right)\tilde{\Psi}_m + \tilde{q}m^2\tilde{\Psi}_m + \tilde{g}_0\tilde{n}_{\rm tot}\tilde{\Psi}_m + \tilde{g}_2\sum_{n=-1}^{1}\tilde{\boldsymbol{F}}\cdot(\hat{\boldsymbol{F}})_{mn}\tilde{\Psi}_n. \tag{E2}$$

Since we are interested in traveling solitons in a uniform system, we assume $\tilde{\mathcal{V}} = \tilde{q} = 0$ and switch to the moving frame with velocity $\tilde{V}$, where the moving-frame time-independent GPEs [34] take the forms

$$\tilde{\mu}\tilde{\Psi}_m = \left(-\frac{1}{2}\frac{\partial^2}{\partial\tilde{z}^2} + i\tilde{V}\frac{\partial}{\partial\tilde{z}}\right)\tilde{\Psi}_m + \tilde{g}_0\tilde{n}_{\rm tot}\tilde{\Psi}_m + \tilde{g}_2\sum_{n=-1}^{1}\tilde{\boldsymbol{F}}\cdot(\hat{\boldsymbol{F}})_{mn}\tilde{\Psi}_n. \tag{E3}$$

To numerically find stationary magnetic soliton solutions of Eq. (E3) we use the Newton-Raphson method which has been used to obtain dipolar solitons or a vortex in a moving frame [33–35]. The simulation is performed on a 1D line $\tilde{z} \in [-40, 40]$ discretized into $\mathcal{N} = 4096$ girds with spacing $\Delta\tilde{z} = 80/(\mathcal{N}-1)$. The discretized wave function is described by $\tilde{\Psi}_{j,m}$ where $j = 1, 2, \ldots, \mathcal{N}$ denotes the jth grid and $m = 0, \pm 1$ is the magnetic quantum number. Since the real and imaginary parts of the wave function are independent degrees of freedom, we define $\tilde{\Psi}_{j,r,m}$ with $r = 0, 1$, where $\tilde{\Psi}_{j,0,m} = \mathrm{Re}(\tilde{\Psi}_{j,m})$ and $\tilde{\Psi}_{j,1,m} = \mathrm{Im}(\tilde{\Psi}_{j,m})$. Equation (E3) can then be discretized as $\boldsymbol{f}(\tilde{\boldsymbol{\Psi}}) = 0$ where

$$\begin{aligned} f_{j,r,m} = &-\frac{1}{2}\frac{\tilde{\Psi}_{j-1,r,m} - 2\tilde{\Psi}_{j,r,m} + \tilde{\Psi}_{j+1,r,m}}{(\Delta\tilde{z})^2} \\ &+ (2r-1)\tilde{V}\frac{\tilde{\Psi}_{j+1,1-r,m} - \tilde{\Psi}_{j-1,1-r,m}}{2\Delta\tilde{z}} \\ &+ \left(-\tilde{\mu} + \tilde{g}_0\sum_{m',r'}\tilde{\Psi}^2_{j,r',m'}\right)\tilde{\Psi}_{j,r,m} \\ &+ \tilde{g}_2\sum_{m'}(\tilde{F}_{x,j}\hat{F}_{x,mm'} + \tilde{F}_{z,j}\hat{F}_{z,mm'})\tilde{\Psi}_{j,r,m'} \\ &- i(2r-1)\tilde{g}_2\sum_{m'}\tilde{F}_{y,j}\hat{F}_{y,mm'}\tilde{\Psi}_{j,1-r,m'}, \end{aligned} \tag{E4}$$

and where $\tilde{\boldsymbol{F}}_j$ is the discretized spin density evaluated at the jth grid,

$$\begin{aligned} \tilde{\boldsymbol{F}}_j &= \sum_{m',n'=-1}^{1}\tilde{\Psi}^*_{j,m'}(\hat{\boldsymbol{F}})_{m'n'}\tilde{\Psi}_{j,n'} \\ &= \sum_{m',n'=-1}^{1}(\tilde{\Psi}_{j,0,m'} - i\tilde{\Psi}_{j,1,m'})(\hat{\boldsymbol{F}})_{m'n'}(\tilde{\Psi}_{j,0,n'} + i\tilde{\Psi}_{j,1,n'}). \end{aligned} \tag{E5}$$

We impose the Neumann boundary condition such that at the factitious grids $j = 0$ and $j = \mathcal{N}+1$ the wave functions are given by

$$\tilde{\Psi}_{0,r,m} = \tilde{\Psi}_{2,r,m}, \quad \tilde{\Psi}_{\mathcal{N}+1,r,m} = \tilde{\Psi}_{\mathcal{N}-1,r,m}. \tag{E6}$$

Starting from the analytical wave function of a magnetic soliton given in the main text, the Newton-Raphson method solves $\boldsymbol{J}\delta\tilde{\boldsymbol{\Psi}} = -\boldsymbol{f}$ for $\delta\tilde{\boldsymbol{\Psi}}$ to update the wave function as $\tilde{\boldsymbol{\Psi}}_{p+1} = \tilde{\boldsymbol{\Psi}}_p + \delta\tilde{\boldsymbol{\Psi}}$ at each step p, where $\boldsymbol{J}$ is the Jacobian of $\boldsymbol{f}$ with respect to $\tilde{\boldsymbol{\Psi}}$,

$$\begin{aligned} J^{j,r,m}_{k,s,n} &= \frac{\partial f_{j,r,m}}{\partial\tilde{\Psi}_{k,s,n}} \\ &= -\frac{1}{2}\frac{\delta_{j+1,k} - 2\delta_{j,k} + \delta_{j-1,k}}{(\Delta\tilde{z})^2}\delta_{r,s}\delta_{m,n} \\ &\quad + (2r-1)\tilde{V}\frac{\delta_{j+1,k} - \delta_{j-1,k}}{2\Delta\tilde{z}}\delta_{1-r,s}\delta_{m,n} \\ &\quad + \left(-\tilde{\mu} + \tilde{g}_0\sum_{m',r'}\tilde{\Psi}^2_{j,r',m'}\right)\delta_{j,k}\delta_{r,s}\delta_{m,n} \\ &\quad + 2\tilde{g}_0\tilde{\Psi}_{j,r,m}\tilde{\Psi}_{j,s,n}\delta_{j,k} \\ &\quad + \tilde{g}_2(\tilde{F}_{x,j}\hat{F}_{x,mn} + \tilde{F}_{z,j}\hat{F}_{z,mn})\delta_{j,k}\delta_{r,s} \\ &\quad + \tilde{g}_2\sum_{m'}(K_{x,j,s,n}\hat{F}_{x,mm'} \\ &\quad + K_{z,j,s,n}\hat{F}_{z,mm'})\tilde{\Psi}_{j,r,m'}\delta_{j,k} \\ &\quad - i(2r-1)\tilde{g}_2\tilde{F}_{y,j}\hat{F}_{y,mn}\delta_{j,k}\delta_{1-r,s} \\ &\quad - i(2r-1)\tilde{g}_2\sum_{m'}K_{y,j,s,n}\hat{F}_{y,mn}\tilde{\Psi}_{j,1-r,m'}\delta_{j,k}, \end{aligned} \tag{E7}$$

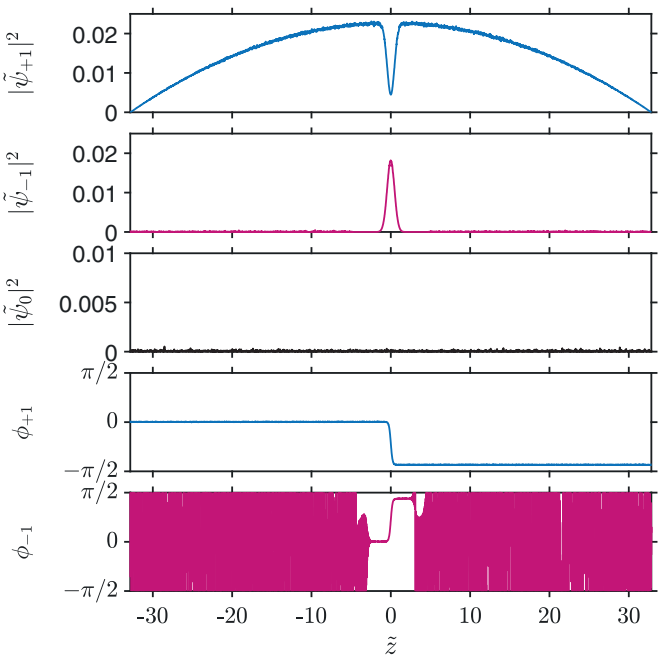

FIG. 5. Initial state for generating a magnetic soliton.

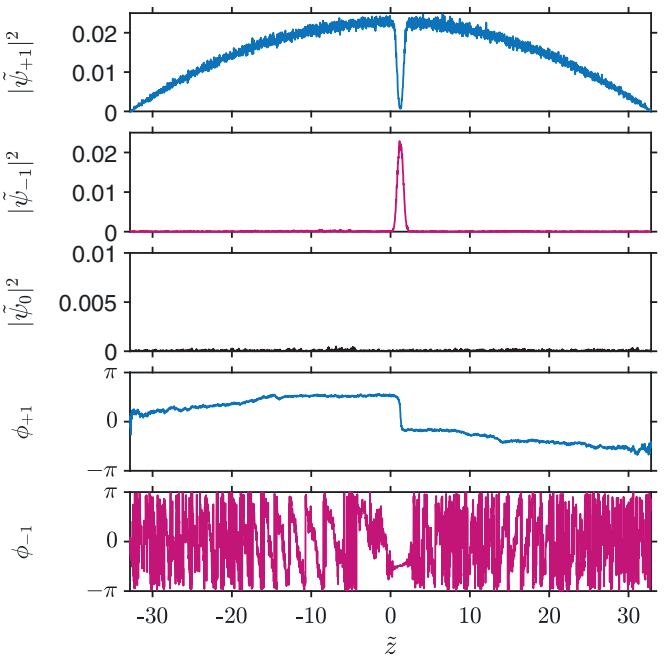

FIG. 6. Density and phase profiles at $\tilde{t} = 3.77$.

and where

$$\boldsymbol{K}_{j,s,n} = \sum_{n'} \{[(\hat{\boldsymbol{F}})_{n,n'} + (\hat{\boldsymbol{F}})^*_{n,n'}]\tilde{\Psi}_{j,s,n'} - i(2s-1)[(\hat{\boldsymbol{F}})_{n,n'} - (\hat{\boldsymbol{F}})^*_{n,n'}]\tilde{\Psi}_{j,1-s,n'}\}. \quad \text{(E8)}$$

Since the atom number is fixed in our simulation, at each step we update the chemical potential $\tilde{\mu}$ according to Eq. (E3). Such an iteration can converge at a final wave function $\tilde{\boldsymbol{\Psi}}_f$ satisfying $\boldsymbol{f}(\tilde{\boldsymbol{\Psi}}_f) = \boldsymbol{0}$, which is the true magnetic soliton solution we seek to obtain. The convergence is determined once the correction $|\delta\tilde{\boldsymbol{\Psi}}|$ is smaller than an arbitrary tolerance.

APPENDIX F: EXPERIMENTAL GENERATION

As discussed in the main text, we propose to use a Raman transition followed by a magnetic shadow (phase imprinting) to generate a magnetic soliton in a quasi-1D ^{87}Rb condensate. To simulate this method, we prepare the initial condition and evolve the wave function as follows:

(1) We assume the population transfer is local and has a Gaussian shape. We also assume that the phase imprinting results in a tanh-shaped phase step. Then the initial state without noise is given by

$$\begin{pmatrix} \tilde{\varphi}_{+1}(\tilde{z}) \\ \tilde{\varphi}_0(\tilde{z}) \\ \tilde{\varphi}_{-1}(\tilde{z}) \end{pmatrix} = \tilde{\psi}_g(\tilde{z}) \begin{pmatrix} \sqrt{1 - Be^{-\tilde{z}^2/2C^2}}\, e^{-i\phi_A(\tilde{z})} \\ 0 \\ \sqrt{Be^{-\tilde{z}^2/2C^2}}\, e^{i\phi_A(\tilde{z})} \end{pmatrix}, \quad \text{(F1)}$$

where $\tilde{\psi}_g(\tilde{z})$ is the ground-state wave function obtained from the imaginary-time propagation method. The phase function is given as

$$\phi_A(\tilde{z}) = \frac{D}{2}\left(\tanh\frac{\tilde{z}}{E} + 1\right). \quad \text{(F2)}$$

In our simulation we use the following dimensionless parameters,

$$B = 0.8, \quad C = 0.463, \quad D = 1.37, \quad E = 0.216. \quad \text{(F3)}$$

For comparison, the dimensionless spin healing length in our simulation is $\tilde{\xi}_s = 0.316$ evaluated at the center of the condensate.

(2) Then we include noise to the initial condition as

$$\tilde{\psi}_{+1}(\tilde{z}) = \tilde{\varphi}_{+1}(\tilde{z})\{1 + \eta_1(\tilde{z}) + i\eta_2(\tilde{z})\}, \quad \text{(F4)}$$

$$\tilde{\psi}_0(\tilde{z}) = \tilde{\varphi}_0(\tilde{z}) + \eta_3(\tilde{z}) + i\eta_4(\tilde{z}), \quad \text{(F5)}$$

$$\tilde{\psi}_{-1}(\tilde{z}) = \tilde{\varphi}_{-1}(\tilde{z})\{1 + \eta_5(\tilde{z}) + i\eta_6(\tilde{z})\} + \alpha(\tilde{z})\{\eta_7(\tilde{z}) + i\eta_8(\tilde{z})\}, \quad \text{(F6)}$$

where $\alpha(\tilde{z}) = 0$ for $-5 < \tilde{z} < 5$ and $\alpha(\tilde{z}) = 1$ otherwise. $\eta_j(\tilde{z})$ is Gaussian noise sampled with the standard deviation 0.005. The initial density distributions and phase profiles are shown in Fig. 5.

(3) We then numerically solve Eq. (D1) with time step $\Delta\tilde{t} = 1.885 \times 10^{-4}$. A quadratic shift $\tilde{q} = -10$ is added to stabilize the condensate. The resultant magnetic soliton resembles the ideal case of no noise as shown in Fig. 6.

[1] R. Camassa and D. D. Holm, Phys. Rev. Lett. **71**, 1661 (1993).
[2] Y. S. Kivshar and G. P. Agrawal, *Optical Solitons: From Fibers to Photonic Crystals* (Academic, San Diego, 2003).
[3] B. J. Carr and E. Verdaguer, Phys. Rev. D **28**, 2995 (1983).
[4] S. S. P. Parkin, M. Hayashi, and L. Thomas, Science **320**, 190 (2008).

[5] S. Burger, K. Bongs, S. Dettmer, W. Ertmer, K. Sengstock, A. Sanpera, G. V. Shlyapnikov, and M. Lewenstein, Phys. Rev. Lett. **83**, 5198 (1999).
[6] L. Khaykovich, F. Schreck, G. Ferrari, T. Bourdel, J. Cubizolles, L. D. Carr, Y. Castin, and C. Salomon, Science **296**, 1290 (2002).
[7] S. V. Manakov, Sov. Phys. JETP **38**, 248 (1974).
[8] T. Busch and J. R. Anglin, Phys. Rev. Lett. **87**, 010401 (2001).
[9] C. Becker, S. Stellmer, P. Soltan-Panahi, S. Dörscher, M. Baumert, E.-M. Richter, J. Kronjäger, K. Bongs, and K. Sengstock, Nat. Phys. **4**, 496 (2008).
[10] H. E. Nistazakis, D. J. Frantzeskakis, P. G. Kevrekidis, B. A. Malomed, and R. Carretero-González, Phys. Rev. A **77**, 033612 (2008).
[11] P. Kevrekidis and D. Frantzeskakis, Rev. Phys. **1**, 140 (2016).
[12] T. M. Bersano, V. Gokhroo, M. A. Khamehchi, J. D'Ambroise, D. J. Frantzeskakis, P. Engels, and P. G. Kevrekidis, Phys. Rev. Lett. **120**, 063202 (2018).
[13] S. Lannig, C.-M. Schmied, M. Prüfer, P. Kunkel, R. Strohmaier, H. Strobel, T. Gasenzer, P. G. Kevrekidis, and M. K. Oberthaler, Phys. Rev. Lett. **125**, 170401 (2020).
[14] E. Timmermans, Phys. Rev. Lett. **81**, 5718 (1998).
[15] D. S. Hall, M. R. Matthews, J. R. Ensher, C. E. Wieman, and E. A. Cornell, Phys. Rev. Lett. **81**, 1539 (1998).
[16] S. Coen and M. Haelterman, Phys. Rev. Lett. **87**, 140401 (2001).
[17] X. Yu and P. B. Blakie, Phys. Rev. Research **3**, 023043 (2021).
[18] H.-J. Miesner, D. M. Stamper-Kurn, J. Stenger, S. Inouye, A. P. Chikkatur, and W. Ketterle, Phys. Rev. Lett. **82**, 2228 (1999).
[19] K. Kasamatsu and M. Tsubota, Phys. Rev. Lett. **93**, 100402 (2004).
[20] C. Qu, L. P. Pitaevskii, and S. Stringari, Phys. Rev. Lett. **116**, 160402 (2016).
[21] X. Chai, D. Lao, K. Fujimoto, R. Hamazaki, M. Ueda, and C. Raman, Phys. Rev. Lett. **125**, 030402 (2020).
[22] A. Farolfi, D. Trypogeorgos, C. Mordini, G. Lamporesi, and G. Ferrari, Phys. Rev. Lett. **125**, 030401 (2020).
[23] X. Chai, D. Lao, K. Fujimoto, and C. Raman, Phys. Rev. Res. **3**, L012003 (2021).
[24] K. Fujimoto, R. Hamazaki, and M. Ueda, Phys. Rev. Lett. **122**, 173001 (2019).
[25] T. Congy, A. Kamchatnov, and N. Pavloff, SciPost Phys. **1**, 006 (2016).
[26] E. G. M. van Kempen, S. J. J. M. F. Kokkelmans, D. J. Heinzen, and B. J. Verhaar, Phys. Rev. Lett. **88**, 093201 (2002).
[27] M. O. D. Alotaibi and L. D. Carr, Phys. Rev. A **96**, 013601 (2017).
[28] G. C. Katsimiga, J. Stockhofe, P. G. Kevrekidis, and P. Schmelcher, Phys. Rev. A **95**, 013621 (2017).
[29] A. Sartori and A. Recati, Eur. Phys. J. D **67**, 260 (2013).
[30] Y. Kawaguchi and M. Ueda, Phys. Rep. **520**, 253 (2012).
[31] A. Kosevich, B. Ivanov, and A. Kovalev, Phys. Rep. **194**, 117 (1990).
[32] P. G. Kevrekidis, H. Nistazakis, D. J. Frantzeskakis, B. A. Malomed, and R. Carretero-González, Eur. Phys. J. D **28**, 181 (2004).
[33] M. J. Edmonds, T. Bland, D. H. J. O'Dell, and N. G. Parker, Phys. Rev. A **93**, 063617 (2016).
[34] T. Winiecki, Numerical studies of superfluids and superconductors, Ph.D. thesis, Durham University, 2001.
[35] T. Winiecki, J. F. McCann, and C. S. Adams, Europhys. Lett. **48**, 475 (1999).
[36] L. Pitaevskii and S. Stringari, *Bose-Einstein Condensation and Superfluidity* (Oxford University Press, Oxford, UK, 2016).
[37] R. Nath, P. Pedri, and L. Santos, Phys. Rev. Lett. **101**, 210402 (2008).
[38] V. V. Konotop and L. Pitaevskii, Phys. Rev. Lett. **93**, 240403 (2004).
[39] K. C. Wright, L. S. Leslie, and N. P. Bigelow, Phys. Rev. A **77**, 041601(R) (2008).
[40] K. Fujimoto, R. Hamazaki, and M. Ueda, Phys. Rev. Lett. **120**, 073002 (2018).